

Europa's H₂O₂: Temperature Insensitivity and a Correlation with CO₂

PEIYU WU ¹, SAMANTHA K. TRUMBO ^{2,3}, MICHAEL E. BROWN ⁴, AND KATHERINE DE KLEER ⁴

¹*Department of Earth and Atmospheric Sciences, Cornell University, Ithaca, NY 14853, USA*

²*Cornell Center for Astrophysics and Planetary Science, Cornell University, Ithaca, NY 14853, USA*

³*Department of Astronomy & Astrophysics, University of California, San Diego, La Jolla, CA 92093, USA*

⁴*Division of Geological and Planetary Sciences, California Institute of Technology, Pasadena, CA 91125, USA*

(Accepted PSJ)

ABSTRACT

H₂O₂ is part of Europa's water-ice radiolytic cycle and a potential source of oxidants to Europa's subsurface ocean. However, factors controlling the concentration of this critical surface species remain unclear. Though laboratory experiments suggest that Europa's H₂O₂ should be concentrated in the coldest, most ice-rich regions toward the poles, Keck adaptive optics observations have shown the strongest H₂O₂ signatures in comparatively warm, salt-bearing terrain at low latitudes. As a result, it was suggested that the local non-ice composition of these terrains—particularly hypothesized enrichments of CO₂—may be a more dominant control on H₂O₂ than temperature or water-ice abundance. Here, we use observations of Europa from the NASA Infrared Telescope Facility, Keck Observatory, and JWST to disentangle the potential effects of temperature and composition. In order to isolate the effect of temperature on Europa's H₂O₂, we use the ground-based observations to assess its response to temperature changes over timescales associated with Europa's daily eclipse and diurnal cycle. We use JWST Cycle 1 data to look for any geographic correlation between Europa's H₂O₂ and CO₂. Both changes in Europa's 3.5- μ m H₂O₂ absorption band from pre to post eclipse and across a local day suggest minimal effects of the local temperature on these timescales. In contrast, the JWST observations show a strong positive correlation between Europa's H₂O₂ and CO₂ bands, supporting the previously suggested possibility that the presence of CO₂ in the ice may enhance H₂O₂ concentrations via electron-scavenging.

Keywords: Galilean satellites (627), Planetary surfaces (2113), Surface composition (2115), Europa (2189), Infrared spectroscopy (2285)

1. INTRODUCTION

Hydrogen peroxide (H₂O₂) is a product of the important water-ice radiolytic cycle on Europa and was first detected by the Galileo Near-Infrared Mapping Spectrometer (NIMS) via a prominent absorption band at 3.5 μ m (Carlson et al. 1999). The continuous bombardment of Europa's surface by electrons, protons, and ions from the Jovian magnetosphere leads to the dissociation of water molecules and the recombination of the fragments to form H₂O₂, molecular oxygen (O₂), and thus an oxidized surface environment (Johnson & Quickenden

1997; Cooper et al. 2003; Johnson et al. 2003; Loeffler et al. 2006; Bain & Giguère 1955; Carlson et al. 1999, 2009). Surface oxidants such as H₂O₂, if transported through Europa's ice shell, could interact with ocean water that is potentially reduced by hydrothermal processes at the seafloor. Such mixing could create a redox potential, providing a viable chemical energy source for Europa's interior ocean (Hand et al. 2006, 2009; Pasek & Greenberg 2012; Chyba 2000). Understanding what controls H₂O₂ can affect our understanding of its stability and how likely it is to get recycled into the interior. It also has implications for the production and stability of related radiolysis products, such as O₂ (Cooper et al. 2003), that are produced by the same or similar processes, but harder to observe. H₂O₂, O₂, and H₂ formation from ion and electron irradiated water ice is

expected to be a common radiation chemistry pathway throughout the outer solar system.

Laboratory spectral measurements and irradiation experiments have been used to understand the radiolysis and photolysis of water ice, including the production and destruction of H_2O_2 (e.g., Cassidy et al. 2010; Hand & Carlson 2011; Johnson & Quickenden 1997; Loeffler et al. 2006; Moore & Hudson 2000). In addition to water ice and sufficient irradiation being essential precursors for H_2O_2 formation, irradiation experiments have also shown an inverse relationship between the equilibrium abundances of H_2O_2 and the ice temperature (Hand & Carlson 2011; Loeffler et al. 2006; Moore & Hudson 2000; Zheng et al. 2006). Thus, it was expected that Europa should have an enrichment of H_2O_2 in colder, more ice-rich regions, compared to a more minimal presence in warmer, less ice-rich regions (Hand & Carlson 2011).

However, contrary to the laboratory predictions, recent Keck AO observations of Europa’s 3.5- μm H_2O_2 absorption feature across its leading hemisphere showed enhanced H_2O_2 in geologically young, low-latitude chaos terrains characterized by lower water-ice abundance (Brown & Hand 2013; Fischer et al. 2015, 2016), warmer temperatures (Rathbun et al. 2010; Trumbo et al. 2018), and a notable enrichment of sodium chloride (NaCl) (Trumbo et al. 2019a, 2022). This observation finds contradictory results on the effects of both water-ice availability and temperature. While the findings indicate that temperature is not the dominant factor, it remains uncertain whether temperature plays a role at all in governing Europa’s H_2O_2 .

In fact, the distribution suggests that the underlying composition of the chaos terrain exerts a stronger control on H_2O_2 abundance. Thus, the authors hypothesized that carbon dioxide (CO_2) may be enhanced in these same terrains (Trumbo et al. 2019b), where it may act to enhance H_2O_2 concentrations by inhibiting the breakdown of newly formed H_2O_2 by consuming the destructive electrons produced as the ice continues to be irradiated (Moore & Hudson 2000)—an effect supported at the time by only limited laboratory data (Moore & Hudson 2000; Strazzulla et al. 2005) and unpublished Galileo NIMS spectra (Carlson 2001). However, this hypothesis remains untested due to the lack of reliable CO_2 mapping on Europa and the inability to observe it from the ground, leaving the effects of temperature and composition on Europa’s H_2O_2 largely unresolved.

To further investigate the effects of temperature and CO_2 on Europa’s H_2O_2 concentrations, we analyze a combination of ground- and space-based observations of Europa’s H_2O_2 from the the NASA Infrared Telescope Facility (IRTF), Keck Observatory, and JWST.

Using IRTF/SpeX, we take disk-integrated observations Europa’s 3.5- μm H_2O_2 absorption before and after eclipse, which preserves approximately the same geometry across a large temperature change, enabling a largely controlled test of possible temperature effects. To examine the reaction of H_2O_2 to temperature fluctuations across longer, diurnal timescales, we present spatiotemporally resolved observations across Europa’s day acquired using the Keck II telescope’s Near InfraRed Spectrograph (NIRSPEC) and adaptive optics (AO) system. Finally, we use spatially-resolved JWST Cycle 1 NIRSpec observations of Europa, which simultaneously span wavelengths sensitive to both H_2O_2 and CO_2 , to search for the previously hypothesized correlation between these two species.

2. OBSERVATIONS AND DATA REDUCTION

2.1. *Disk-integrated Pre- and post-eclipse IRTF/SpeX observations*

To disentangle the effect of temperature on Europa’s H_2O_2 from that of composition, we designed a controlled temperature experiment using disk-integrated spectra obtained in one-hour windows across two hours pre-eclipse and six hours post-eclipse with SpeX (Rayner et al. 2003) at the NASA Infrared Telescope Facility (IRTF) across several dates with similar eclipse windows in 2018. The SpeX data obtained span a wavelength range of 1.68–4.23 μm with $R \sim 2,000$. Dates, time, and geometries are given in Table 1.

Depending on the exact thermal inertia of the surface materials, an eclipse leads to a sudden temperature drop of 10s of degrees Kelvin, while the satellite maintains approximately the same geometry as viewed from Earth. (Figure 1A). As simple extrapolation from laboratory studies suggests a ~ 20 K temperature drop may increase the equilibrium band area of the H_2O_2 absorption by approximately a factor of ~ 4 (Hand & Carlson 2011), we assessed changes in Europa’s H_2O_2 absorption band immediately before and after eclipse and throughout this recovery period to look for such a response. As Europa is tidally locked to Jupiter and experiences an eclipse of its sub-Jovian hemisphere every orbit, pre- and post-eclipse spectra taken on different dates are still sampling the same temperature drop and recovery (Table 1). Our data cover the wavelength range of ~ 1.68 -4.2 μm . For pre-eclipse observations, we observed HD 140990, a $V = 7.85$ G2V star with a 7.08° separation from Europa, as the telluric calibrator. For post-eclipse observations, we observed HD 128596, a $V = 7.48$ G2V star with a 2.45° separation from Europa, as the telluric calibrator.

We used Spextool (Spectral Extraction TOOL), an Interactive Data Language (IDL)-based data reduction

Table 1. Table of Observations

Date (UT)	Telescope	Hemisphere	Slit Orientation	Airmass Range	Integration (Minutes)	Central Longitude	Central Latitude	Star Calibrator
2018 Mar 29	IRTF/Spex	Sub-Jovian ^a	Disk-integrated	1.3	32	345 W	4 S	HD 140990
2018 Mar 29	IRTF/Spex	Sub-Jovian ^b	Disk-integrated	1.3-1.4	48	348 W	4 S	HD 140990
2018 May 11	IRTF/Spex	Sub-Jovian ^c	Disk-integrated	1.2-1.3	32	11 W	4 S	HD 128596
2018 May 11	IRTF/Spex	Sub-Jovian ^d	Disk-integrated	1.2	40	14 W	4 S	HD 128596
2018 Jun 30	IRTF/Spex	Sub-Jovian ^e	Disk-integrated	1.2	8	29 W	4 S	HD 128597
2018 Jun 30	IRTF/Spex	Sub-Jovian ^f	Disk-integrated	1.2	43	31 W	4 S	HD 128597
2018 Jun 30	IRTF/Spex	Sub-Jovian ^g	Disk-integrated	1.2-1.3	33	36 W	4 S	HD 128597
2018 Jun 30	IRTF/Spex	Sub-Jovian ^h	Disk-integrated	1.3-1.5	38	39 W	4 S	HD 128597
2013 Dec 29	Keck AO	Anti-Jovian	E/W	1.0-1.2	40	195 W	3 N	HD 54371
2013 Dec 29	Keck AO	Anti-Jovian	E/W	1.1	20	195 W	25 S	HD 54372
2016 Feb 24	Keck AO	Trailing/sub-Jovian	E/W	1.5-1.7	40	334 W	2 S	HD 98947
2016 Feb 24	Keck AO	Trailing/sub-Jovian	E/W	1.2-1.3	40	338 W	0 N	HD 98947
2016 Feb 24	Keck AO	Trailing/sub-Jovian	E/W	1.0-1.1	40	342 W	1 S	HD 98947
2016 Feb 24	Keck AO	Sub-Jovian	N/S	1	40	350 W	2 S	HD 98947
2016 Feb 24	Keck AO	Sub-Jovian	N/S	1	40	348 W	2 S	HD 98947
2016 Feb 25	Keck AO	Leading	E/W	1.2-1.4	40	79 W	0 S	HD 98947
2016 Feb 25	Keck AO	Leading	E/W	1.1-1.2	40	82 W	12 S	HD 98947
2016 Feb 25	Keck AO	Leading	N/S	1.0-1.1	40	88 W	2 S	HD 98947
2016 Feb 25	Keck AO	Leading	E/W	1.1	40	95 W	0 N	HD 98947
2018 Jun 06	Keck AO	Leading	E/W	1.5	20	115 W	7 S	HD 128596
2018 Jun 06	Keck AO	Leading	N/S	1.4	10	120 W	5 S	HD 128596
2018 Jun 06	Keck AO	Leading	N/S	1.4	10	126 W	5 S	HD 128596
2018 Jun 06	Keck AO	Leading/anti-Jovian	N/S	1.2-1.3	20	171 W	2 S	HD 128596
2018 Jun 06	Keck AO	Leading/anti-Jovian	N/S	1.2-1.3	20	150 W	2 S	HD 128596
2018 Jun 06	Keck AO	Leading/anti-Jovian	N/S	1.3	10	166 W	1 S	HD 128596
2018 Jun 06	Keck AO	Leading	N/S	1.2	15	113 W	4 S	HD 128596
2018 Jun 06	Keck AO	Leading	N/S	1.2-1.3	20	100 W	6 S	HD 128596
2018 Jun 06	Keck AO	Leading	N/S	1.3	20	82 W	3 S	HD 128596
2018 Jun 06	Keck AO	Leading	E/W	1.3-1.4	20	131 W	1 S	HD 128596
2018 Jun 07	Keck AO	Trailing	E/W	1.2-1.3	40	222 W	4 S	HD 128596
2021 Sep 24	Keck AO	Trailing	E/W	1.2-1.4	60	275 W	20 N	HD 203311
2021 Sep 25	Keck AO	Trailing	N/S	1.3-1.4	40	318 W	8 N	HD 203311
2021 Sep 25	Keck AO	Sub-Jovian/Leading	N/S	1.3	40	41 W	2 N	HD 203311
2022 Nov 23	JWST	Leading	-	-	21	93 W	3 N	GSPC P330-E

[a] 2 hours pre-eclipse; [b] 1 hour pre-eclipse; [c] 1 hour post-eclipse; [d] 2 hours post-eclipse; [e] 3 hours post-eclipse; [f] 4 hours post-eclipse; [g] 5 hours post-eclipse; [h] 6 hours post-eclipse

package (Cushing et al. 2004), to reduce the IRTF/Spex data. We followed the standard methodology of flat field correction, image pair subtraction, target detection, spectra extraction, wavelength calibration, combination of multi-order spectra, and telluric correction (Vacca et al. 2003). Spectra from within each 1-hour window were merged into one single spectrum per window. We clipped out bad pixels and any highly variable telluric lines by comparing data points to the means of a

51-point window with a threshold of 0.01, as determined by manually inspecting the spectra so that only telluric lines and outliers are clipped. To further improve the signal-to-noise ratio, we then smoothed the spectra using a Savitzky-Golay filter with a window length of 5 data points and a polynomial order of 3.

Though the geometry was nearly identical between subsequent time windows, Europa did rotate ~ 50 degrees in longitude across the entire 8 hours of observa-

tion. To address this caveat, we used spatially resolved Keck AO observations of the sub-Jovian hemisphere to estimate the effects of small changes in observed band strength attributable to the minor amount of rotation in the eclipse experiment.

2.2. Spatially resolved Keck AO observations across Europa’s day

The creation and destruction of H_2O_2 on Europa exists in a dynamic equilibrium, and the timescale for response to a temperature perturbation is unknown. Indeed, the factor of ~ 4 change in H_2O_2 band strength from laboratory studies mentioned above is a direct comparison of H_2O_2 band strengths in pure water ice at different temperatures irradiated until equilibrium concentrations were achieved (Hand & Carlson 2011), which is not directly translatable to Europa. Thus, we also evaluate the response of H_2O_2 to temperature variations across a longer timescale than eclipse by using Keck NIRSPEC and the AO system on the Keck II telescope to observe Europa’s 3.5- μm H_2O_2 band throughout its day.

We observed the same locations on rotational timescales from 4 hours (comparable in timeframe to Europa’s eclipse recovery) to 29 hours ($\sim 1/3$ Europa day and equivalent to progression from morning to afternoon) and assessed their localized diurnal variability. In addition, we observed some locations that expand on past maps of the spatial distribution of Europa’s H_2O_2 (Trumbo et al. 2019b). Observations used in this analysis were acquired in 2013, 2016, 2018, and 2021. Dates, times, and geometries are given in Table 1. We used the $3.96'' \times 0.072''$ slit in low-resolution mode ($R = 2000$) across the L band wavelengths of approximately 3.1–4 μm .

In 2013, we used HD 54371, a $V = 7.1$ G6V star at 3.2° separation from Europa, as the telluric calibrator. Each telluric calibrator pointing consisted of 1 12-20s coadd or 2 15s coadds. In 2016, we used HD 98947, a $V = 6.9$ G5 star at 1.2° separation from Europa, as the telluric calibrator. Each telluric calibrator pointing consisted of 2 15s coadds. In 2018, we used HD 128596, a $V = 7.5$ G2V star with a 3.9° separation from Europa. Each telluric calibrator pointing consisted of 2 10s coadds. In 2021, we used HD 203311, a $V = 7.45$ G2V star with a 5.15° separation from Europa. Each telluric calibrator pointing consisted of 2 15s coadds.

We obtained ephemeris data and viewing geometry from JPL Horizons. During the observations, Europa’s apparent diameter was approximately $1''$, translating to about 10 resolution elements (~ 300 km resolution at the sub-observer point) at the diffraction limit of Keck at 3.5

μm . We shifted the pointing of targets between opposite ends along the slits in an AB, ABBA, or ABBAAB pattern, to enable pair-subtraction during reduction. Corresponding slit-viewing camera (SCAM) images were acquired to ensure a consistent slit position across each observation set and to allow for later determination of the corresponding geographic coordinates on Europa.

Some of the observations displayed readout artifacts (artificial brightening of every 8 or 64 pixels in the dispersion direction), which we replaced with the mean of the two immediately adjacent pixels. Following the data reduction outlined in Trumbo et al. (2019b), we then used Python packages (astropy (Robitaille et al. 2013; Price-Whelan et al. 2018, 2022), scikit-image (van der Walt et al. 2014), scipy (Virtanen et al. 2020), cartopy (Met Office 2010 - 2015), astroquery (Ginsburg et al. 2019)) in following the standard reduction steps of image rectification, flat field correction, image pair subtraction, residual sky subtraction, spectra extraction, and telluric calibration. We used an ATRAN atmospheric transmission spectrum (Lord 1992) for wavelength calibration. The first several columns of the flatfields (separate from the target’s location on the chip) were consistently unevenly illuminated, so we replaced the unilluminated edge with the mean of the adjacent illuminated window of the same width in pixels.

We extracted summed spectra in 8-pixel resolution elements, stepping by 4 spatial pixels. As with the IRTF spectra, we clipped out bad pixels and any highly variable telluric lines by comparing data points to the means of a 51-point window with a threshold adjusted for each observation. Spectra were then smoothed using a Savitzky-Golay filter with an optimal window length and a polynomial order of 3 to improve signal-to-noise.

To estimate the coordinates of the slit on Europa and extract spectra for each resolution element, we aligned SCAM images to each NIRSPEC exposure. With detector resolutions of $0.013''/\text{pixel}$ (pre-upgrade NIRSPEC), $0.009''/\text{pixel}$ (updated NIRSPEC after 2018), $0.0168''/\text{pixel}$ (pre-upgrade SCAM), and $0.0149''/\text{pixel}$ (updated SCAM), we calculated the size of Europa in both NIRSPEC and SCAM pixels. We then located Europa in the 2D spectral images and estimated the coordinates of the slit by calculating the slit pixel offsets from Europa’s center in the SCAM images. With the known NIRSPEC pixel scale, we determined the geographic coordinates of each resolution element. When combining individual exposures (from A and B nods), we account for small changes to the effective slit width that result from minor shifts in the pointing on Europa. We estimate the spatial uncertainty from our SCAM navigation procedure to be one SCAM pixel, which is much smaller

than the $\sim 0.09''$ diffraction limit of Keck at $3.5 \mu\text{m}$. We use the extracted coordinates to map the geographic distribution of the $3.5\text{-}\mu\text{m}$ H₂O₂ band. For overlapping regions, we averaged band strengths. We excluded data from limb pixels in the trailing hemisphere slits, where the data quality was too poor to reliably measure the H₂O₂ band.

2.3. Spatially resolved JWST observation

As CO₂ has been proposed as a potential factor enhancing H₂O₂ concentrations in chaos terrains (Trumbo et al. 2019b; Carlson 2001; Carlson et al. 2009), we assessed the correlation between the geographic distribution of Europa's H₂O₂ and CO₂ using archival JWST NIRSpec data (from the Cycle 1 Guaranteed Time Observations program #1250) of Europa's leading hemisphere, observed on November 23, 2022, at 08:18 UT. The data we analyzed were obtained with the NIRSpec integral field unit (IFU), the high-resolution gratings (G235H and G395H, R = 2700), and the F170LP and F290LP filters at wavelengths of approximately $1.7\text{--}5.2 \mu\text{m}$. Only Europa's leading hemisphere (sub-observer longitude of 93°W) was observed during this program. We used a spectrum of GSPC P330-E (Program 1538 (Gordon et al. 2022)), a G0V star, as a solar analog. We followed the same data reduction steps as in Trumbo & Brown (2023) and Trumbo et al. (2023) for both the Europa data and the stellar data, and extracted spectra corresponding to each $0.1'' \times 0.1''$ spatial pixel on Europa.

2.4. Band strength calculation

To assess the response of Europa's H₂O₂ to temperature changes and its potential correlation with CO₂, we measure the strength of the $3.5\text{-}\mu\text{m}$ H₂O₂ feature in all extracted spectra from IRTF, Keck, and JWST. For all spectra, we excluded the absorption feature itself ($3.4\text{--}3.65 \mu\text{m}$) before fitting a second-order polynomial across the wavelength range of 3.37 to $3.715 \mu\text{m}$. Each fit was visually inspected, and minor adjustments were made as needed to ensure an optimal fit to the continuum. We then divided the fitted continuum from each spectrum to isolate the absorption feature. Band areas (i.e. equivalent widths) were calculated by integrating the area of the residual absorption.

CO₂ displays three signatures in the JWST data—a narrow band near $2.7 \mu\text{m}$ and two minima within the ν_3 band at $\sim 4.25 \mu\text{m}$ and $4.27 \mu\text{m}$ (Trumbo & Brown 2023; Villanueva et al. 2023). To assess the correlation with our H₂O₂ measurements, we used published band areas of the ν_3 band from (Trumbo & Brown 2023), separately calculated the band depths of each ν_3 minimum relative

to the continua fit by those authors, and calculated the area of the $2.7\text{-}\mu\text{m}$ band by simply fitting and removing a linear continuum. We excluded some pixels close to Europa's limb that appeared particularly affected by flux-oscillation artifacts resulting from the instrument's undersampling of the point spread function. These oscillations significantly impact areas where Europa's signal changes rapidly (Trumbo & Brown 2023). Oscillations affected the measurement of the $3.5\text{-}\mu\text{m}$ H₂O₂ feature in more pixels than that of the CO₂ feature, which resulted in the exclusion of a few more pixels than Trumbo & Brown (2023).

3. PRE- AND POST-ECLIPSE H₂O₂ MEASUREMENTS

To isolate the effect of temperature on Europa's H₂O₂ from those of composition or geography, we measure the $3.5\text{-}\mu\text{m}$ H₂O₂ band on Europa's sub-Jovian hemisphere across a 2-hour period before eclipse and across a 6-hour period following the conclusion of its daily eclipse. Using the thermal model of Trumbo et al. (2017b) and the best-fit thermal inertia value ($60 \text{ J}/(\text{m}^2\text{Ks}^{1/2})$) found in Trumbo et al. (2018) from ALMA observations of the sub-Jovian hemisphere, we estimate an expected $\sim 20 \text{ K}$ temperature drop across eclipse and a recovery to pre-eclipse temperatures that span the 6-hour post-eclipse period across which we observed. (Figure 1A).

Hand & Carlson (2011) irradiated pure water ice with 10 keV electrons at temperatures of 80 K , 100 K , and 120 K and monitored the change in H₂O₂ band absorption until equilibrium concentrations were achieved at flux levels of $\sim 10^{19} \text{ eV cm}^{-2}$. The authors' measured equilibrium H₂O₂ band area at 120 K is approximately a factor of 4 weaker than the measured equilibrium H₂O₂ band area at 100 K and a factor of 6 weaker than the measured equilibrium H₂O₂ band area at 80 K . This laboratory result is consistent with the expected increased mobility of OH with increasing temperature (Johnson & Quickenden 1997; Hand & Carlson 2011; Loeffler et al. 2006; Quickenden et al. 1991). Though, it is worth noting that the magnitude of temperature effects seen in laboratory studies varies, with some experiments (e.g., Gomis et al. 2004; Loeffler et al. 2006; Zheng et al. 2006) observing smaller changes in H₂O₂ concentration than Hand & Carlson (2011) and some modeling work predicting smaller effects as well (Teolis et al. 2017). Nevertheless, taking the most simplistic extrapolation from these experiments, we might expect up to a factor of 4 increase in our observed H₂O₂ band area immediately after the $\sim 20\text{-K}$ eclipse temperature drop and then a slow decrease of the absorption band as the temperature climbs back up toward pre-eclipse values.

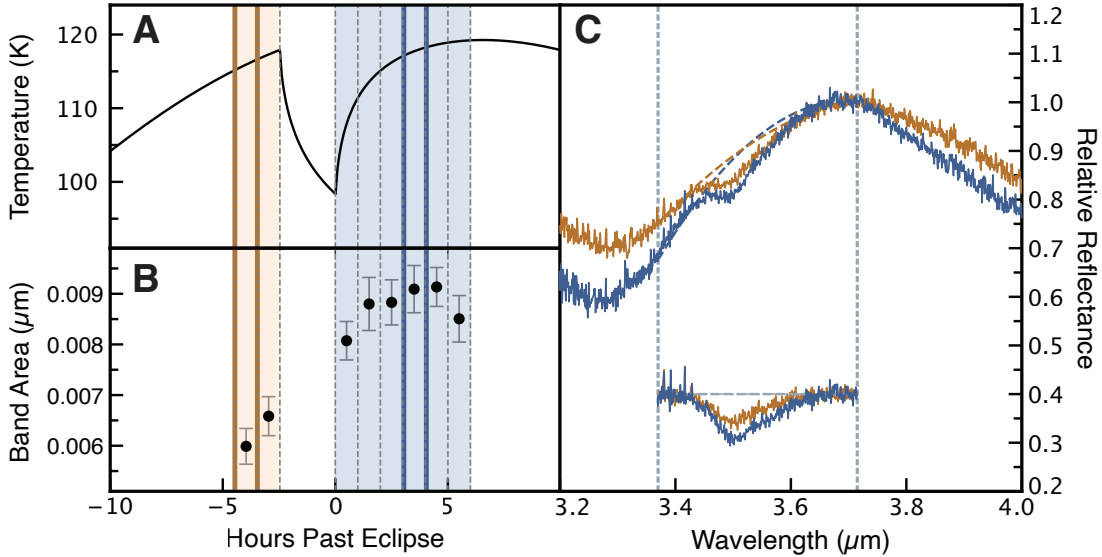


Figure 1. [A] The temperature of sub-Jovian Europa as it passes through eclipse. This temperature profile is based on the thermal model of (Trumbo et al. 2017a). Sub-Jovian Europa was observed for 2 hours before eclipse and 6 hours after eclipse (no observations during eclipse due to the lack of reflected light). The bottom of the drop indicates the end of eclipse. The sub-Jovian temperature takes ~ 6 hours to recover from the estimated ~ 20 K drop during eclipse. Spectra were averaged for each of the ~ 1 -hour time intervals. Orange indicates pre-eclipse observations and blue indicates post-eclipse observations. [B] Integrated band area calculated for each ~ 1 -hour window. A factor of < 2 change is observed both between the measurements immediately pre-eclipse and immediately post-eclipse, and between the weakest $3.5\text{-}\mu\text{m}$ absorption at 2 hours pre-eclipse and the strongest $3.5\text{-}\mu\text{m}$ absorption 5 hours post-eclipse. This small change is attributable to rotation of Europa across this time period and rules out a strong response to the eclipse temperature drop (discussed in section 3). As errors associated with the unknown background continuum dominate over those due to noise, we estimate error bars as the values given using a range of plausible continuum fits across the wavelength range from $3.33\text{--}3.37\ \mu\text{m}$ to $3.715\text{--}3.78\ \mu\text{m}$. [C] Example IRTF/Spex spectra comparing the $3.5\text{-}\mu\text{m}$ absorption 2-hours pre-eclipse with the absorption 4-hours post-eclipse. The boundaries of the selected time windows are bold in [B]. Dashed gray lines outline the H_2O_2 band. Second-order polynomial continua are indicated by the dashed curves of the same color as the spectra. Continuum-removed absorptions are included to ease comparison of the band strengths. The depth of the $3\text{-}\mu\text{m}$ water ice absorption band (shown here as the $3.2\text{--}3.7\ \mu\text{m}$ range following the Fresnel peak) appears to increase after eclipse (blue), suggesting a possible rotational effect as Europa rotates from a more trailing/sub-Jovian geometry towards a more sub-Jovian/leading geometry.

In Figure 1B, we plot H_2O_2 band areas of the averaged spectra from each 1-hour time window surrounding the eclipse, where the error bars are estimated by varying the continuum fits across the wavelength range from $3.33\text{--}3.37\ \mu\text{m}$ to $3.715\text{--}3.78\ \mu\text{m}$. The unknown true continuum presents a larger source of error than noise, but our error bars are still far smaller than the large increases in band strength we seek to detect. All of the spectra used to derive the band areas in Figure 1 are included in Figure A1. We find that our data clearly rule out such a dramatic increase in the H_2O_2 band following eclipse, instead exhibiting only a small 22.6% change (factor of 1.23) between the measurements immediately pre-eclipse and immediately post-eclipse, and a 38.7% change (factor of 1.53) between the weakest $3.5\text{-}\mu\text{m}$ absorption at 2 hours pre-eclipse and the strongest $3.5\text{-}\mu\text{m}$ absorption 5 hours post-eclipse.

It is possible that this small change does reflect a delayed response to the eclipse temperature drop resulting from the unknown timescale needed for Europa’s surface H_2O_2 concentrations to re-equilibrate. However, the 2- and $3\text{-}\mu\text{m}$ water-ice absorption bands also appear to change following the eclipse and across the recovery period, which suggests that Europa’s small degree of rotation from the slightly less-icy trailing/sub-Jovian geometry pre-eclipse (central longitude = 348°W) towards a slightly more-icy sub-Jovian/leading geometry (central longitude = 36°W) by 5 hour post-eclipse needs to be considered as well. Our spatially resolved Keck observation across the sub-Jovian hemisphere suggests up to a factor of ~ 2.1 increase in H_2O_2 band strength as the longitude shifts from 352°W to 33°W degrees. Thus, the small change (factor < 2) of H_2O_2 band strength following eclipse could be reasonably attributed to the

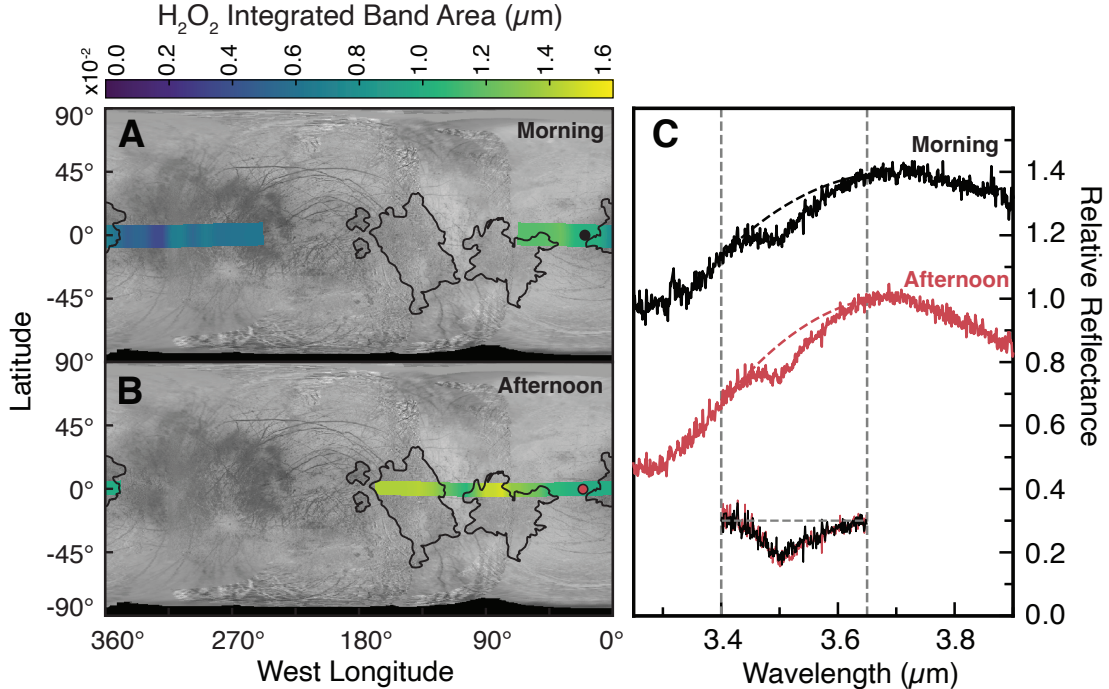


Figure 2. [A] Example Keck NIRSPEC slit obtained on February 24, 2016, when 18.6°W (labeled with the black dot) is in the morning (~ 13 hours prior to local noon in Europa’s ~ 85 -hour day, estimated ~ 103 K). [B] Example Keck NIRSPEC slit obtained on February 25, 2016, when the same region (18.5°W; labeled with the red dot) is in the afternoon (~ 16 hours after local noon in Europa’s ~ 85 -hour day, estimated ~ 115 K). [C] Corresponding reflectance spectra for this location in the morning (in black) and in the afternoon (in red). Dashed gray lines outline the H₂O₂ band. Second-order polynomial continua are indicated by the dashed curves of the same color as the spectrum. Continuum-removed absorptions are included and show nearly overlapping absorptions. A ~ 12 K temperature increase over 24 hours is estimated from the thermal model of [Trumbo et al. \(2017a\)](#). This temperature change results in a negligible -3.1% change in the integrated band areas. Leading chaos regions are outlined in black ([Leonard et al. 2024](#)). Background basemap credit: [USGS \(2002\)](#).

~ 50 degrees of rotation of Europa surrounding eclipse, and our eclipse experiment reveals no clear evidence for any response of Europa’s H₂O₂ to the temperature changes across eclipse, let alone the large factors seen in laboratory experiments. However, it is possible that the unknown time it would take Europa’s H₂O₂ to re-equilibrate following such a perturbation is longer than the eclipse experiment allowed.

4. KECK H₂O₂ DIURNAL VARIABILITY

While we find no clear effect of temperature in our IRTF eclipse experiment, the laboratory data that see strong differences in H₂O₂ with temperature represent a direct comparison of equilibrium concentrations (e.g., [Hand & Carlson 2011](#)), which may not have been reached across the eclipse timescale. For this reason, we also use Keck NIRSPEC AO observations to look for variability in Europa’s H₂O₂ over longer, diurnal timescales. In particular, we examine slits oriented in an east/west direction that cover the same surface regions at different times of the local day. As noted above,

[Hand & Carlson \(2011\)](#) suggest that equilibrium abundances of H₂O₂ can vary by a factor of 4 across the 100-120 K temperature range relevant to Europa and that H₂O₂ can be destroyed during the day in equatorial regions and produced efficiently at night across the surface, such that higher H₂O₂ concentration might be expected in the early morning as opposed to in the warm afternoon.

During our 2016 and 2018 observations, we purposely aligned slits taken on adjacent nights to investigate the hypothesized diurnal variability of H₂O₂. We examine 5 east-west slit pairs centered within $\pm 20^\circ$ of the equator, spanning a timescale of 20-29 hours—approximately one-quarter to one-third of a Europa day—and covering the temperature progression from morning to afternoon. Similar to what we see from the eclipse experiment, the changes in integrated band area from morning to afternoon appear to be much smaller than the equilibrium variations observed in the lab and instead range from -32% to 30% (factor of 0.68–1.3), with no clear or consistent trend attributable to diurnal variability.

As a representative example, in Figure 2, we compare spectra of the same location (18.6°W, 0.4°N) observed in the morning (cold temperatures) and afternoon (warmer temperatures) of February 2016. Using the thermal model of Trumbo et al. (2017a) and a thermal inertia of 60 J/(m²Ks^{1/2}) suggested by ALMA observations of the sub-Jovian hemisphere (Trumbo et al. 2018) and consistent with thermal inertia values estimated from the Galileo Photopolarimeter-Radiometer (PPR) observations (Spencer et al. 1999; Rathbun et al. 2010), we estimate a corresponding ~12 K temperature increase over a ~24-hour timescale for this location. We observe only a minimal change (-3.1%) in the integrated H₂O₂ band areas for this location, and, indeed, the entirety of the overlapping portions of the two slits appear consistent. All of the overlapping E/W slit positions we inspect are presented in Figure A2.

To expand on this analysis, we also assess 2 east/west slit pairs observed over a timescale of 4 and 16 hours between 2013 and 2018 (rather than subsequent nights) in our larger dataset (Figure A2). We observe only minimal changes in integrated band areas from -0.24% to 0.44% (factor of 0.76-1.44). We also note that there appears to be some evidence for stochastic H₂O₂ variability between years, as noted in Trumbo et al. (2019b), where the bands observed in 2016 are overall stronger than in later years (Figure A2). We suggest that this could be related to potential variability of the dynamic radiation environment.

The lack of a strong or consistent diurnal trend, along with the minimal changes observed across eclipse, suggest that Europa’s H₂O₂ is largely insensitive to the temperature fluctuations that it experiences on a daily basis. Thus, our results indicate that, in addition to temperature not influencing the spatial variations of Europa’s H₂O₂, temperature also appears not to drive strong temporal variations. We discuss this apparent discrepancy with laboratory work further in section 7.

5. KECK H₂O₂ MAPPING

In addition to suggesting that diurnal temperature changes do not strongly control Europa’s H₂O₂, the Keck observations provide additional spatial coverage of Europa’s surface compared to past maps of H₂O₂ (Trumbo et al. 2019b). In Figure 3, we present maps of H₂O₂ band area composed of east/west orientated and north/south oriented slits from 2013, 2016, 2018, and 2021, which include additional coverage beyond the previous maps. We separated out coverage of the leading and trailing hemispheres for clarity, and to highlight the longitudinal variation along the two included anti-Jovian E/W slits. Overall, the updated distribu-

tion agrees well with the trends shown by Trumbo et al. (2019b).

Our maps present a clear difference between low-latitude chaos and low-latitude plains terrain in east/west slits crossing the leading chaos regions (Figure 2B, Figure 3A, Figure A2A-D), and a north/south slit just east of Tara Regio (~85° W) (Figure 3A) shows overall weaker H₂O₂ absorption and less latitudinal variation in H₂O₂ than do north/south slits crossing Tara Regio. This distribution further confirms the curious enrichment of the 3.5- μ m H₂O₂ feature within the large-scale chaos terrains at low-to-mid-latitudes on the leading hemisphere (Trumbo et al. 2019b), which are understood to contain endogenic non-ice material like salts (Fischer et al. 2015, 2016; Trumbo et al. 2019a, 2022).

Our maps also provide additional north/south and east/west coverage on the trailing hemisphere. Given the drastic changes in the spectral continuum shape between the two hemispheres associated with changes in water-ice abundance, we carefully inspected all continuum-fitting manually and adjusted fitting parameters accordingly. Consistent with the hemispheric data of Hand & Brown (2013) and the spatially resolved data of Trumbo et al. (2019b), the trailing regions show much weaker H₂O₂ absorption overall. This hemispheric difference in H₂O₂ abundance may stem from the strong contrast in water ice fraction between the leading and trailing hemispheres (Trumbo et al. 2019b; Hand & Brown 2013). The widespread SO₂ on the trailing hemisphere (e.g., Becker et al. 2022) may also contribute to the depletion of H₂O₂ via interactions to create sulfate (Trumbo et al. 2019b; Loeffler & Hudson 2013).

As the H₂O₂ absorption on the trailing hemisphere is so weak against the background continuum, we cannot robustly distinguish between trailing chaos and non-chaos regions or make a clear detection of any latitudinal trend on this hemisphere. However, we do repeatedly see a depletion of H₂O₂ west of the anti-Jovian point around 210°W, which corresponds to a gap between the large-scale chaos regions of the leading and trailing hemispheres (Figure 3, Figure A2), hinting that similar geological associations could exist below our detection across the trailing side. This depletion around 210° W also corresponds to lower mean reflectances across the L-band (3.15 to 3.95 μ m) mapped in Fischer et al. (2016). Future, high-signal-to-noise JWST observations of Europa’s trailing hemisphere would help further investigate the geographic variation of its weak H₂O₂ bands.

With the additional Keck coverage, we confirm a strong correlation between concentrated H₂O₂ and chaos terrains. This suggests that the endogenic composition of these regions may play an important role in

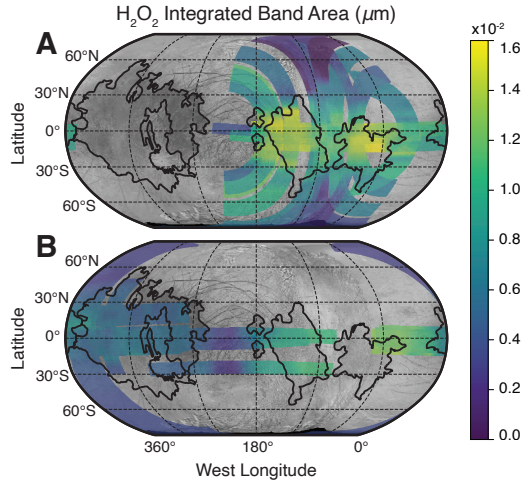


Figure 3. Mapped Keck NIRSPEC slits from our 2013, 2016, 2018, and 2021 observations on the leading [A] and trailing [B] hemispheres, which show the spatial distribution of Europa’s 3.5- μm H₂O₂ band. Consistent with full-disk spectra (Hand & Brown 2013) and previous spatially resolved spectra (Trumbo et al. 2019b), the geologically young chaos regions on the leading hemisphere (outlined in black; Leonard et al. 2024) exhibit the largest H₂O₂ features. In contrast, the trailing hemisphere demonstrates generally much weaker absorptions compared to the leading hemisphere and a depletion of H₂O₂ west of the anti-Jovian point around 210°W, corresponding to a gap between the large-scale chaos regions of the leading and trailing hemispheres. We note that observations from various years are mapped together to illustrate the updated coverage of Europa’s H₂O₂, despite some apparently stochastic fluctuations in H₂O₂ between 2016 and later years. Background basemap credit: USGS (2002).

controlling the distribution of H₂O₂ and that a possible correlation with CO₂ remains a key hypothesis (Trumbo et al. 2019b).

6. JWST MAPPING AND CORRELATION WITH CO₂

To investigate the hypothesized effect of CO₂ on the unexpected distribution of H₂O₂ (Trumbo et al. 2019b), we measure the H₂O₂ band in the Cycle 1 JWST data recently used to map Europa’s leading-hemisphere CO₂ (Trumbo & Brown 2023; Villanueva et al. 2023) and evaluate whether H₂O₂ and CO₂ are geographically correlated. Both features are observed simultaneously in the same dataset, ensuring the best geographic alignment.

In Figure 4A, we map the integrated band areas of the 3.5- μm H₂O₂ feature across Europa’s leading hemisphere and show the corresponding map of Europa’s ν_3 CO₂ band, as obtained by Trumbo & Brown

(2023) (Figure 4B). In agreement with the Keck observations (Trumbo et al. 2019b, this work), we find that the strongest H₂O₂ absorption occurs in the leading-hemisphere chaos terrains Tara Regio ($\sim 85^\circ$ W) and Powys Regio ($\sim 125^\circ$ W) (Figure 4A), which also exhibit the strongest CO₂ signatures (Figure 4B). In fact, a simple linear fit between the H₂O₂ and CO₂ band strengths in the JWST data reveals a strong positive correlation (Pearson correlation coefficient of 0.94), as would be expected for the previously hypothesized effect of endogenic CO₂ on radiolytically produced H₂O₂ (Figure 4C).

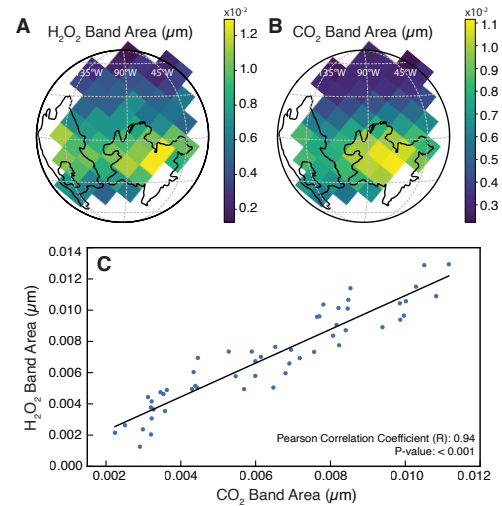


Figure 4. [A] Map of the H₂O₂ integrated band area from the JWST Cycle 1 observations. Gray dashed lines indicate the meridians and the 60° S, 30° S, 0° N, 30° N, and 60° N parallels. The strongest absorption occurs in Tara Regio ($\sim 85^\circ$ W) to the right of the 90° W meridian and in parts of the chaos region Powys Regio ($\sim 125^\circ$ W) on the left portion of the disk. [B] Map of the entire ν_3 CO₂ integrated band area (μm) (Trumbo & Brown 2023). Concentrated CO₂ occurs in the same regions as concentrated H₂O₂—the leading chaos terrains. The disk of Europa is indicated by a black circle centered at 2.7°N, 93°W. [C] Linear fit illustrating the relationship between the distributions of the two features. A Pearson correlation coefficient of 0.94 ($P < 0.001$) signifies a strong positive correlation between the distributions of H₂O₂ and CO₂ on the leading hemisphere. Consistent with Trumbo & Brown (2023), limb pixels affected by the instrument’s inherent undersampling of the point spread function are excluded. Oscillations affected the measurement of the 3.5- μm H₂O₂ feature in more pixels than that of the CO₂ feature. Therefore, a few more pixels are excluded than in Trumbo & Brown (2023). Leading chaos regions are outlined in black (Leonard et al. 2024).

Two distinct peaks are resolved within the ν_3 band of Europa’s CO₂ (at 4.25 μm and at 4.27 μm) (Trumbo

& Brown 2023), along with a combination band at 2.7 μm (Villanueva et al. 2023). As these signatures might indicate different CO_2 host materials or trapping mechanisms, we also assess the correlation of H_2O_2 with the individual depths of each CO_2 peak within the ν_3 band and with the strength of the 2.7- μm feature. The Pearson correlation coefficients (R) calculated with respect to the 4.25- μm peak, the 4.27- μm peak, and the 2.7- μm band—with coefficients of 0.92 ($P < 0.001$), 0.92 ($P < 0.001$), and 0.90 ($P < 0.001$), respectively—are consistent with that calculated with respect to the overall ν_3 band ($R = 0.94$; $P < 0.001$). As all three CO_2 signatures are individually the strongest within Tara Regio ($\sim 85^\circ$ W) and Powys Regio ($\sim 125^\circ$ W) (Trumbo & Brown 2023; Villanueva et al. 2023), it is unsurprising that we cannot separate a correlation between H_2O_2 and a particular CO_2 phase from a simple strong correlation with the overall abundance of CO_2 regardless of its trapping mechanisms or host materials. Nevertheless, the strong pixel-to-pixel correspondence suggests that the presence of CO_2 in some form may be an important factor affecting the distribution of H_2O_2 in the chaos terrains, though the possibility remains that H_2O_2 could be associated with chaos terrains for an independent reason.

7. DISCUSSION

Our findings suggest that Europa’s H_2O_2 is largely insensitive to the daily temperature changes it experiences. We find no strong evidence to support the idea that H_2O_2 builds up efficiently overnight, and then becomes depleted across Europa’s day, as hypothesized from laboratory work demonstrating an inverse dependence of equilibrium H_2O_2 concentrations on ice temperature (Hand & Carlson 2011). We suggest that this apparent discrepancy might be due to the short timescales of Europa’s temperature changes, though we also note that the observed magnitude of the influence of temperature also varies widely across different irradiation experiments and may be part of the explanation as well (e.g., Gomis et al. 2004; Loeffler et al. 2006; Zheng et al. 2006). Indeed, conditions directly analogous to Europa’s diurnal cycles have, to our knowledge, not been simulated in the lab, and the timescale for the reaction of the dynamic equilibrium of production and destruction of H_2O_2 in impure ice to temperature perturbations is uncertain. Hand & Carlson (2011) infer that, if starting from pristine ice (with no H_2O_2 or other non-ice materials, like CO_2) and irradiating at a constant surface temperature (as was done in their experiments), it would take an estimated ~ 48 hours of irradiation on the trailing hemisphere and approximately two weeks on the leading hemisphere to reach equilibrium (Hand

& Carlson 2011; Carlson et al. 2009). These timescales are extremely short in geologic terms, suggesting that a dynamic equilibrium with respect to H_2O_2 is almost instantly achieved following any resurfacing events, but they do not directly enable precise predictions of diurnal variations. Future irradiation experiments that first reach equilibrium H_2O_2 concentrations and then continuously monitor changes in H_2O_2 absorption, while simulating the temperature fluctuations observed on Europa through controlled heating and cooling, could help further investigate the timescales needed for Europa’s H_2O_2 to respond to local temperature changes.

Though our IRTF and Keck results contradict the hypothesized temperature effects, our JWST results showing a strong correlation between H_2O_2 and CO_2 within large-scale, leading-hemisphere chaos regions support the previously proposed hypothesis that CO_2 may be an important factor controlling the geographic distribution of H_2O_2 on Europa (Trumbo et al. 2019b). Certain laboratory experiments have shown that electron-accepting contaminants, such as O_2 and CO_2 , have the potential to enhance H_2O_2 yields (Moore & Hudson 2000; Strazzulla et al. 2005), potentially by inhibiting the breakdown of newly formed H_2O_2 by consuming the destructive electrons produced as the ice continues to be irradiated (Moore & Hudson 2000). Indeed, recent work continues to build on these prior experiments and appears to confirm the augmenting effects of small amounts of CO_2 more robustly (Mamo et al. 2023; Raut et al. 2024), which further suggests that the spatial correlation between Europa’s CO_2 and H_2O_2 reflects this effect, rather than coincidence.

Though CO_2 may explain the surprising association of radiolytically produced H_2O_2 with endogenic terrains on the leading hemisphere, it remains unclear how important it is for the trailing side. It is possible that the lower water-ice fraction (e.g., Brown & Hand 2013; Fischer et al. 2015; Ligier et al. 2016) and warmer temperatures (e.g., Rathbun et al. 2010; Trumbo et al. 2018) on the trailing side may help explain its comparative lack of H_2O_2 . The potential chemical reaction with SO_2 (Loeffler & Hudson 2013) also remains a compelling possibility. As there are few existing constraints on the possibility of CO_2 on Europa’s trailing hemisphere (Carlson et al. 2009; Hansen & McCord 2008), the magnitude of its influence relative to these other effects remains an open question. Future JWST observations of the trailing side would help further explore the H_2O_2 - CO_2 -chaos connection and in the context of the added complications of sulfur radiolysis (e.g., Carlson et al. 2002, 2009).

H_2O_2 was recently discovered on Ganymede and was found to be associated with its cold, icy, and highly ir-

radiated polar regions (Trumbo et al. 2023). This discovery contrasts with the distribution of Europa's H₂O₂ in warm, ice-poor, large-scale chaos terrains at low-to-mid latitudes, and instead aligns better with laboratory expectations on the effects of water-ice availability, temperature, and irradiation (e.g., Zheng et al. 2006; Loeffler et al. 2006; Moore & Hudson 2000; Hand & Carlson 2011). Indeed, Ganymede's equatorial latitudes, where little H₂O₂ is observed, are shielded from irradiation by its intrinsic magnetic field (e.g., Khurana et al. 2007; Poppe et al. 2018) and are warmer than Europa's equator (e.g., Orton et al. 1996; Spencer et al. 1999; de Kleer et al. 2021). Thus, though such factors do not seem to control the geographic distribution of H₂O₂ on Europa, they may still be important on Ganymede. Interestingly, however, Ganymede's surface also features ubiquitous CO₂ (e.g., Hibbitts et al. 2003), which JWST data suggest exists in multiple trapped phases across the surface (Bockelée-Morvan, D. et al. 2024). The CO₂ appears most abundant in the equatorial regions, where it is suggested to be trapped in dark and non-icy substrates (Hibbitts et al. 2003; Bockelée-Morvan, D. et al. 2024), which would most likely separate it from the production of H₂O₂ in water ice. However, in the polar regions, the CO₂ may be trapped within amorphous water ice and is spatially coincident with the H₂O₂ (Bockelée-Morvan, D. et al. 2024). This opens up the possibility of a similar influence on H₂O₂ as seems likely on Europa and is consistent with the possibility that CO₂, in addition to the low temperatures, more abundant water ice, and preferential radiolysis driven by Jovian magnetospheric particles, might help enhance H₂O₂ abundances at Ganymede's poles.

JWST observations of Callisto, in contrast, reveal no signs of H₂O₂ (Cartwright et al. 2024), despite its widespread CO₂ (Hibbitts et al. 2000, 2002; Cartwright et al. 2024). The lack of H₂O₂ on Callisto might be related to multiple factors. First, Callisto's surface, although featuring localized bright and ice-rich knobs (Moore et al. 2004), appears to be primarily characterized by a dark, ice-poor lag deposit (Moore et al. 1999; Cartwright et al. 2024), which would restrict the availability of water ice for radiolysis. Moreover, Callisto's distance from Jupiter results in a much weaker impact of charged-particle irradiation on its surface, and the flux of charged particles from Jupiter's magnetosphere is hundreds of times lower than at Europa (Cooper et al. 2001; Johnson et al. 2004). Additionally, Callisto (like Ganymede's equatorial latitudes) has a higher surface temperature (representative equatorial daytime temperature ~155 K) than Europa (representative equatorial daytime temperature of ~120 K) (Spencer et al. 1999;

Camarca et al. 2023; Hanel et al. 1979; Rathbun et al. 2010; Trumbo et al. 2018; Spencer 1987). Collectively, these factors may inhibit the production of H₂O₂ at Callisto to the point where the presence of CO₂ is not enough to result in detectable H₂O₂.

Looking at H₂O₂ across the Galilean system may thus help us understand the factors controlling its presence on each moon. CO₂ appears likely important for H₂O₂, on Europa and potentially also on Ganymede. Surface temperature, while not important for spatial or temporal variations of H₂O₂ on Europa, does align with the influences expected from laboratory studies (e.g., Zheng et al. 2006; Loeffler et al. 2006; Moore & Hudson 2000; Hand & Carlson 2011) when looking at the icy Galilean satellites as a whole. Future JWST observations of the icy satellites of Saturn and icy Kuiper Belt Objects—like Charon (Pluto's largest moon), where both CO₂ and H₂O₂ were recently detected (Protopapa et al. 2023)—may enhance our understanding of the complex interplay of factors influencing the radiolytic production of H₂O₂, thereby providing deeper insights into this important process in the outer solar system.

8. CONCLUSION

In this study, we use a combination of IRTF, Keck, and JWST observations of Europa to assess the influence of temperature and CO₂ on Europa's H₂O₂. We find at most minimal changes in H₂O₂ as a result of local temperature variations on timescales associated with Europa's eclipse by Jupiter and diurnal cycle, suggesting a surprising temperature insensitivity that appears at odds with some laboratory studies. We suggest that this apparent discrepancy might be explained if the diurnal timescales are short compared to those needed for the H₂O₂ concentrations to respond to a temperature perturbation and recommend laboratory experiments to explore this further. Using JWST NIRSpec data, we find a clear and strong correlation between Europa's H₂O₂ and CO₂, supporting the previously suggested hypothesis that endogenic CO₂ may enhance H₂O₂ abundances and thereby explain the unexpected concentration of H₂O₂ in low-latitude chaos terrain. This correlation is also in agreement with limited past and recent laboratory work suggesting that CO₂ can act as an electron-scavenging contaminant that increases H₂O₂ yields by inhibiting its breakdown. Future spatially resolved observations on Europa's trailing hemisphere can further test this correlation and explore the possible influence of sulfur-bearing, trailing-hemisphere components as well.

ACKNOWLEDGMENTS

The IRTF/Spex data presented were obtained at the Infrared Telescope Facility, which is operated by the University of Hawaii under contract 80HQTR19D0030 with the National Aeronautics and Space Administration. The Keck AO data presented were obtained at the W. M. Keck Observatory, which is operated as a scientific partnership among the California Institute of Technology, the University of California, and the National Aeronautics and Space Administration. The Observatory was made possible by the generous financial support of the W. M. Keck Foundation. The authors wish to recognize and acknowledge the very significant cultural role and reverence that the summit of Maunakea has always had within the indigenous Hawaiian community. We are most fortunate to have the opportunity to conduct observations from this mountain. The JWST data were obtained from the Mikulski Archive for Space Telescopes (MAST) at the Space Telescope Science Institute, which is operated by the Association of Universities for Research in Astronomy under NASA contract NAS 5-03127 for JWST. These observations are associated with program #1250. The authors acknowledge H. Hammel and the GTO team led by PI G. Villanueva for developing their observing program with a zero-exclusive-access period. The specific observations analyzed can be accessed via DOI: [10.17909/e269-sm44](https://doi.org/10.17909/e269-sm44). We thank Ryleigh Davis for fruitful discussions and Jonathan Lunine for insightful comments and constructive suggestions. We thank Erin Leonard for providing shape files for Europa's geologic units.

Facilities: IRTF/Spex, Keck AO, JWST

Software: Astropy (Robitaille et al. 2013; Price-Whelan et al. 2018, 2022), Scikit-image (van der Walt et al. 2014), Scipy (Virtanen et al. 2020), Cartopy (Met Office 2010 - 2015), Astroquery (Ginsburg et al. 2019), Spextool (Cushing et al. 2004)

APPENDIX

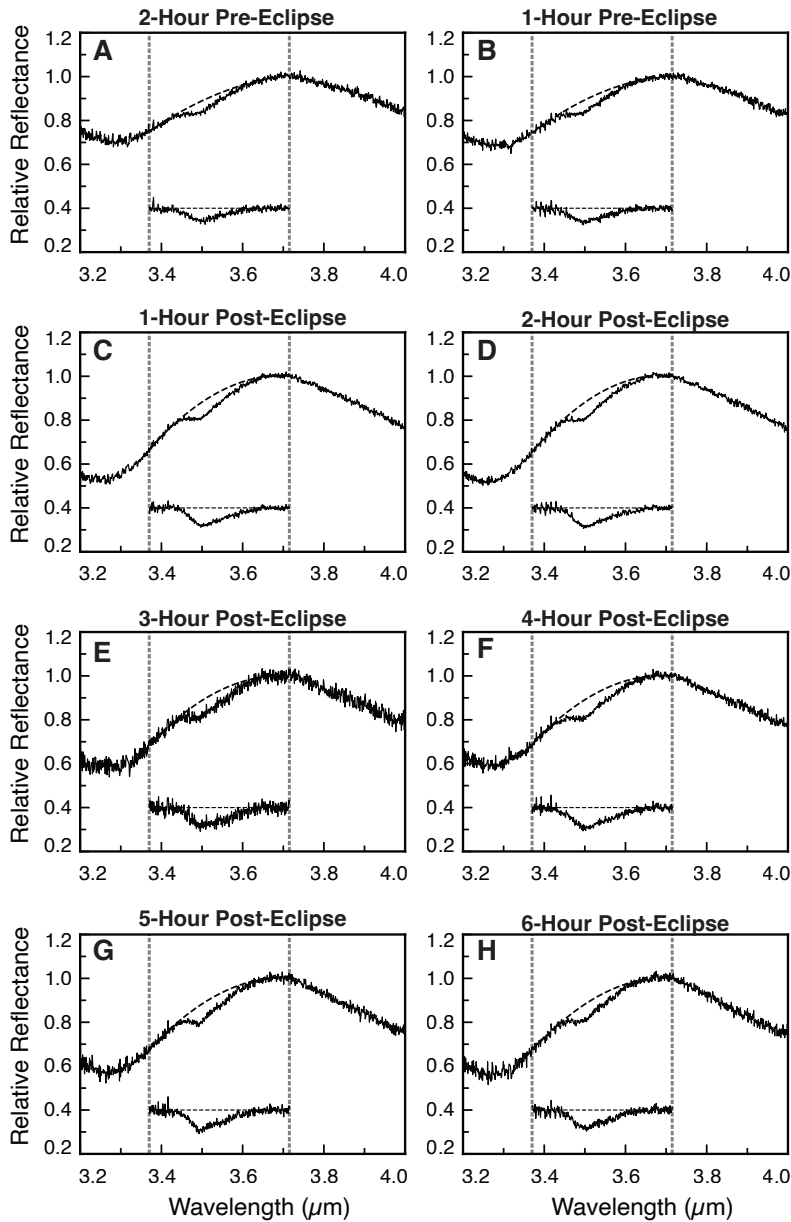


Figure A1. Averaged spectra for each ~ 1 -hour time window of [A] 2 hours pre-eclipse, [B] 1 hour pre-eclipse, [C] 1 hour post-eclipse, [D] 2 hours post-eclipse, [E] 3 hours post-eclipse, [F] 4 hours post-eclipse, [G] 5 hours post-eclipse, and [H] 6 hours post-eclipse. All spectra are normalized to their individual peaks in the $3.6\text{--}3.7\ \mu\text{m}$ region. Dashed gray lines outline the H₂O₂ band. Second-order polynomial continua are indicated by the black dashed curves. Continuum-removed absorptions are included. We note that the 3-hour post-eclipse spectrum is noisier due to a shorter observation time (necessitated by weather conditions), as indicated in Table 1. A factor of change < 2 is shown in the H₂O₂ band throughout the 8-hour time period surrounding eclipse. The slight changes to the background water-ice absorption bands suggest likely rotational effects as Europa rotates from a more trailing/sub-Jovian geometry towards a more sub-Jovian/leading geometry. More discussion is included in section 3.

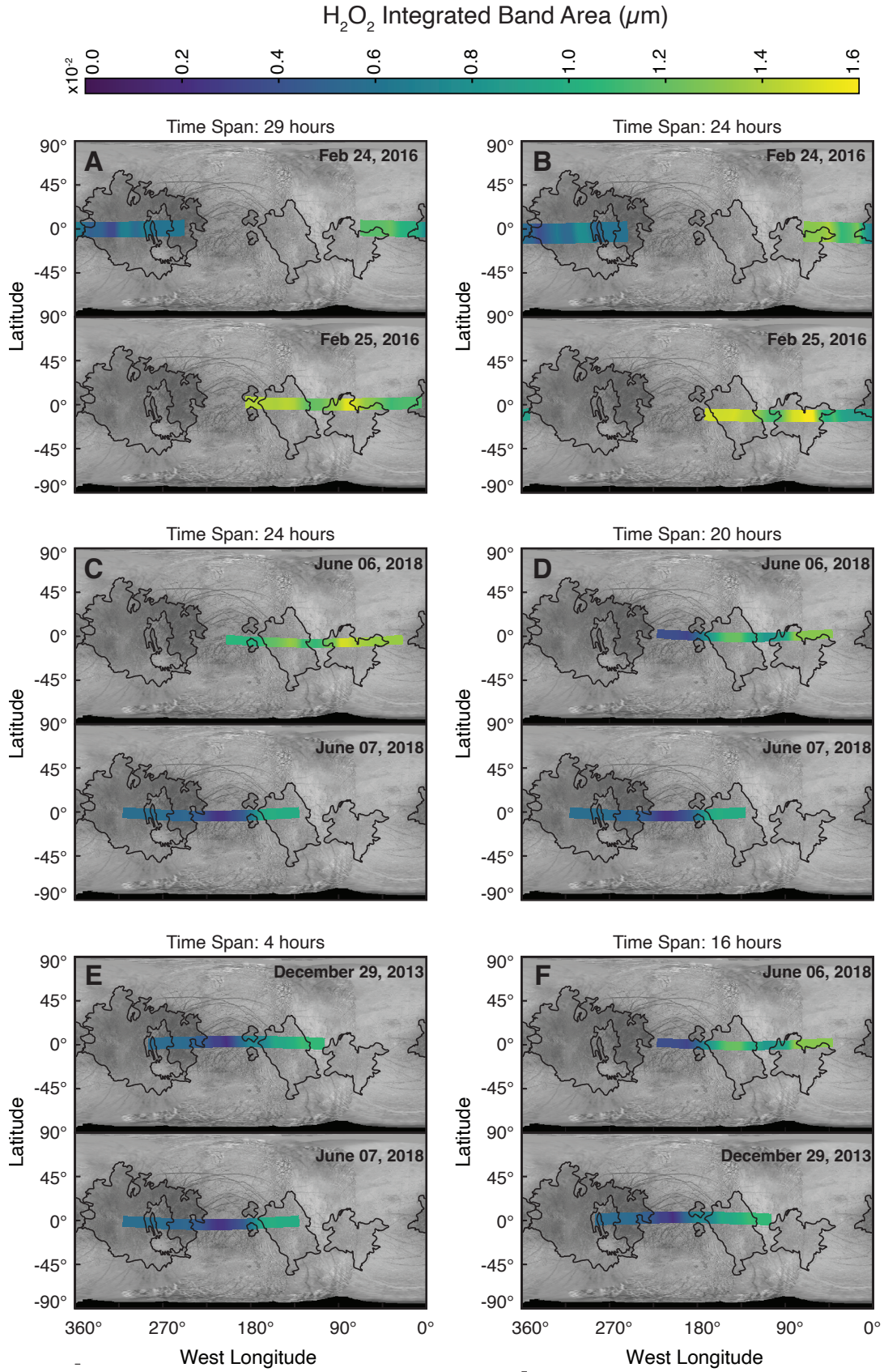


Figure A2. Additional representative paired slits to illustrate the lack of a strong diurnal trend. We examine a total of 5 Keck slit pairs observed on adjacent nights in 2016 and 2018, one of which is shown in Figure 2, and 2 slit pairs observed across different years. Time spans for each paired comparison are labeled on top. [A] Paired slits from consecutive nights obtained on February 24, 2016 [top] and February 25, 2016 [bottom], when overlapped regions ($\sim 18\text{-}36^\circ\text{W}$) are in the morning and afternoon, respectively. [B] Paired slits slightly south of A with a slightly shorter time span, obtained on February 24, 2016 [top] and February 25, 2016 [bottom], when overlapped regions ($\sim 20\text{-}45^\circ\text{W}$) are in the morning and afternoon, respectively. [C] Paired slits obtained from consecutive nights on June 06, 2018 [top] and June 07, 2018 [bottom], when overlapped regions ($\sim 155\text{-}179^\circ\text{W}$) are in the morning and afternoon, respectively. [D] Paired slits from consecutive nights obtained on June 06, 2018 [top] and June 07, 2018 [bottom], when overlapped regions ($\sim 157\text{-}180^\circ\text{W}$) are in the morning and afternoon, respectively. [E] Paired slits obtained across years on December 29, 2013 [top] and June 07, 2018 [bottom], when overlapped regions ($\sim 155\text{-}182^\circ\text{W}$) are in the morning and afternoon, respectively. [F] Paired slits obtained across years on June 06, 2018 [top] and December 29, 2013 [bottom], when overlapped regions ($\sim 155\text{-}181^\circ\text{W}$) are in the morning and afternoon, respectively. For all pairs and overlapping regions examined, the measured band area changes from morning to afternoon are within -32% to 44% (factor of 0.68-1.44). These results suggest the absence of a strong diurnal trend and a lack of sensitivity in H₂O₂ to temperature variations over the assessed time scales. The slits also present a clear difference between low-latitude chaos and low-latitude plains terrain in east/west slits crossing the leading chaos regions [A-D] and a depletion of H₂O₂ west of the anti-Jovian point around 210°W , corresponding to a gap between the large-scale chaos regions of the leading and trailing hemispheres [C-F]. Leading and trailing chaos regions are outlined in black (Leonard et al. 2024). Background basemap credit: USGS (2002).

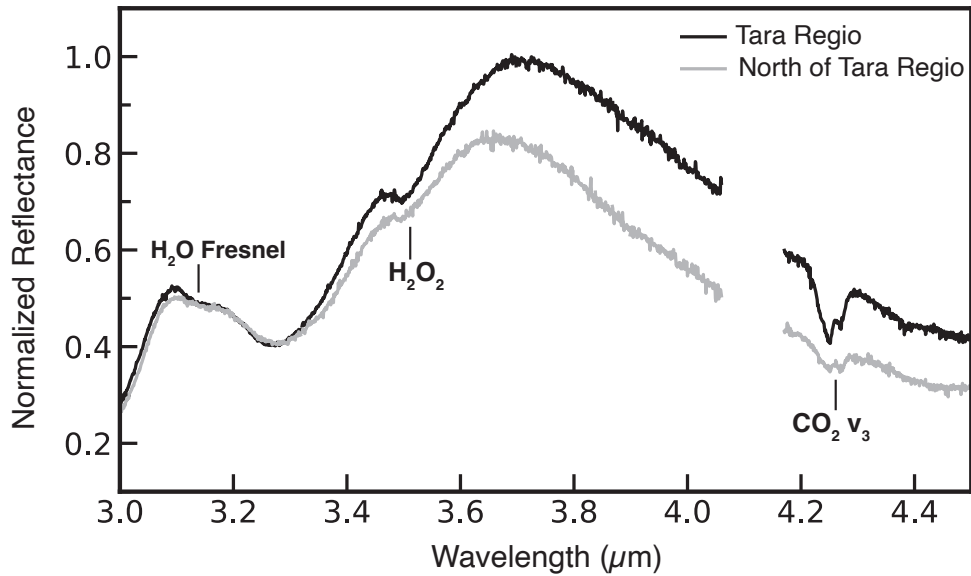


Figure A3. Representative JWST spectra used for Figure 4, showing both the H₂O₂ and the CO₂ bands in the Cycle 1 JWST data recently used to map Europa's leading-hemisphere CO₂ (Trumbo & Brown 2023; Villanueva et al. 2023). The black spectrum is extracted from a pixel within Tara Regio (92°W , 17°S) and the gray spectrum is extracted from a pixel north of Tara Regio (57°W , 19°N). A clear enrichment of both H₂O₂ and CO₂ is shown in the Tara Regio spectrum.

REFERENCES

- Bain, O., & Giguère, P. A. 1955, *Canadian Journal of Chemistry*, 33, 527, doi: [10.1139/v55-063](https://doi.org/10.1139/v55-063)
- Becker, T. M., Trumbo, S. K., Molyneux, P. M., et al. 2022, *The Planetary Science Journal*, 3, 129, doi: [10.3847/PSJ/ac69eb](https://doi.org/10.3847/PSJ/ac69eb)
- Bockelée-Morvan, D., Lellouch, E., Poch, O., et al. 2024, *A&A*, 681, A27, doi: [10.1051/0004-6361/202347326](https://doi.org/10.1051/0004-6361/202347326)
- Brown, M. E., & Hand, K. P. 2013, *The Astronomical Journal*, 145, 110, doi: [10.1088/0004-6256/145/4/110](https://doi.org/10.1088/0004-6256/145/4/110)
- Camarca, M., de Kleer, K., Butler, B., et al. 2023, *The Planetary Science Journal*, 4, 142, doi: [10.3847/PSJ/aceb68](https://doi.org/10.3847/PSJ/aceb68)
- Carlson, R. W. 2001, in *Bulletin of the American Astronomical Society*, Vol. 33, 1125
- Carlson, R. W., Anderson, M. S., Johnson, R. E., Schulman, M. B., & Yavrouian, A. H. 2002, *Icarus*, 157, 456, doi: [10.1006/icar.2002.6858](https://doi.org/10.1006/icar.2002.6858)
- Carlson, R. W., Calvin, W. M., Dalton, J. B., et al. 2009, *Europa*, ed. R. T. Pappalardo, W. B. McKinnon, & K. Khurana (Tucson, AZ: The University of Arizona Press), 283–328
- Carlson, R. W., Johnson, R. E., & Anderson, M. S. 1999, *Science*, 286, 97
- Cartwright, R. J., Villanueva, G. L., Holler, B. J., et al. 2024, *The Planetary Science Journal*, 5, 60, doi: [10.3847/PSJ/ad23e6](https://doi.org/10.3847/PSJ/ad23e6)
- Cassidy, T., Coll, P., Raulin, F., et al. 2010, *Space Science Reviews*, 153, 299, doi: [10.1007/s11214-009-9625-3](https://doi.org/10.1007/s11214-009-9625-3)
- Chyba, C. F. 2000, *Nature*, 403, 381
- Cooper, J. F., Johnson, R. E., Mauk, B. H., Garrett, H. B., & Gehrels, N. 2001, *Icarus*, 149, 133, doi: <https://doi.org/10.1006/icar.2000.6498>
- Cooper, P. D., Johnson, R. E., & Quickenden, T. I. 2003, *Icarus*, 166, 444, doi: <https://doi.org/10.1016/j.icarus.2003.09.008>
- Cushing, M. C., Vacca, W. D., & Rayner, J. T. 2004, *Publications of the Astronomical Society of the Pacific*, 116, 362, doi: [10.1086/382907](https://doi.org/10.1086/382907)
- de Kleer, K., Butler, B., de Pater, I., et al. 2021, *The Planetary Science Journal*, 2, 5
- Fischer, P. D., Brown, M. E., & Hand, K. P. 2015, *The Astronomical Journal*, 150, 164, doi: [10.1088/0004-6256/150/5/164](https://doi.org/10.1088/0004-6256/150/5/164)
- Fischer, P. D., Brown, M. E., Trumbo, S. K., & Hand, K. P. 2016, *The Astronomical Journal*, 153, 13
- Ginsburg, A., Sipőcz, B. M., Basseur, C. E., et al. 2019, *AJ*, 157, 98, doi: [10.3847/1538-3881/aafc33](https://doi.org/10.3847/1538-3881/aafc33)
- Gomis, O., Leto, G., & Strazzulla, G. 2004, *A&A*, 420, 405, doi: [10.1051/0004-6361:20041091](https://doi.org/10.1051/0004-6361:20041091)
- Gordon, K. D., Bohlin, R., Sloan, G. C., et al. 2022, *The Astronomical Journal*, 163, 267, doi: [10.3847/1538-3881/ac66dc](https://doi.org/10.3847/1538-3881/ac66dc)
- Hand, K. P., & Brown, M. E. 2013, *The Astrophysical Journal*, 766, L21, doi: [10.1088/2041-8205/766/2/L21](https://doi.org/10.1088/2041-8205/766/2/L21)
- Hand, K. P., & Carlson, R. W. 2011, *Icarus*, 215, 226, doi: <https://doi.org/10.1016/j.icarus.2011.06.031>
- Hand, K. P., Chyba, C. F., Carlson, R. W., & Cooper, J. F. 2006, *Astrobiology*, 6, 463
- Hand, K. P., Chyba, C. F., Priscu, J. C., Carlson, R. W., & Neelson, K. H. 2009, *Europa*, ed. R. T. Pappalardo, W. B. McKinnon, & K. Khurana (Tucson, AZ: The University of Arizona Press), 589–630
- Hanel, R., Conrath, B., Flasar, M., et al. 1979, *Science*, 206, 952, doi: [10.1126/science.206.4421.952](https://doi.org/10.1126/science.206.4421.952)
- Hansen, G. B., & McCord, T. B. 2008, *Geophysical Research Letters*, 35, doi: [10.1029/2007gl031748](https://doi.org/10.1029/2007gl031748)
- Hibbitts, C. A., Klemaszewski, J. E., McCord, T. B., Hansen, G. B., & Greeley, R. 2002, *Journal of Geophysical Research: Planets*, 107, 14, doi: <https://doi.org/10.1029/2000JE001412>
- Hibbitts, C. A., McCord, T. B., & Hansen, G. B. 2000, *Journal of Geophysical Research: Planets*, 105, 22541, doi: <https://doi.org/10.1029/1999JE001101>
- Hibbitts, C. A., Pappalardo, R. T., Hansen, G. B., & McCord, T. B. 2003, *Journal of Geophysical Research: Planets*, 108, doi: <https://doi.org/10.1029/2002JE001956>
- Johnson, R., Carlson, R., Cooper, J., et al. 2004, *Jupiter: The planet, satellites and magnetosphere*, 485
- Johnson, R. E., & Quickenden, T. I. 1997, *Journal of Geophysical Research: Planets*, 102, 10985
- Johnson, R. E., Quickenden, T. I., Cooper, P. D., McKinley, A. J., & Freeman, C. G. 2003, *Astrobiology*, 3, 823, doi: [10.1089/153110703322736123](https://doi.org/10.1089/153110703322736123)
- Khurana, K. K., Pappalardo, R. T., Murphy, N., & Denk, T. 2007, *Icarus*, 191, 193
- Leonard, E. J., Alex Patthoff, D., & Senske, D. A. 2024, *Global geologic map of Europa*, Report 3513, doi: [10.3133/sim3513](https://doi.org/10.3133/sim3513)
- Ligier, N., Poulet, F., Carter, J., Brunetto, R., & Gourgeot, F. 2016, *The Astronomical Journal*, 151, 163
- Loeffler, M., Raut, U., Vidal, R., Baragiola, R., & Carlson, R. 2006, *Icarus*, 180, 265, doi: <https://doi.org/10.1016/j.icarus.2005.08.001>
- Loeffler, M. J., & Hudson, R. L. 2013, *Icarus*, 224, 257, doi: <https://doi.org/10.1016/j.icarus.2013.02.005>
- Lord, S. D. 1992, *A new software tool for computing Earth's atmospheric transmission of near-and far-infrared radiation*, Vol. 103957 (Ames Research Center)

- Mamo, B., Brody, J., Teolis, B., et al. 2023, *Bulletin of the AAS*, 55
- Met Office. 2010 - 2015, *Cartopy: a cartographic python library with a Matplotlib interface*, Exeter, Devon. <https://scitools.org.uk/cartopy>
- Moore, J. M., Asphaug, E., Morrison, D., et al. 1999, *Icarus*, 140, 294
- Moore, J. M., Chapman, C. R., Bierhaus, E. B., et al. 2004, *Jupiter: The Planet, Satellites, and Magnetosphere*, ed. F. Bagenal, T. E. Dowling, & W. B. McKinnon (Cambridge University Press), 397–426
- Moore, M., & Hudson, R. 2000, *Icarus*, 145, 282, doi: <https://doi.org/10.1006/icar.1999.6325>
- Orton, G., Spencer, J., Travis, L., Martin, T., & Tamppari, L. 1996, *Science*, 274, 389
- Pasek, M. A., & Greenberg, R. 2012, *Astrobiology*, 12, 151, doi: [10.1089/ast.2011.0666](https://doi.org/10.1089/ast.2011.0666)
- Poppe, A., Fatemi, S., & Khurana, K. 2018, *Journal of Geophysical Research: Space Physics*, 123, 4614
- Price-Whelan, A. M., Sipőcz, B. M., Günther, H. M., et al. 2018, *AJ*, 156, 123, doi: [10.3847/1538-3881/aabc4f](https://doi.org/10.3847/1538-3881/aabc4f)
- Price-Whelan, A. M., Lim, P. L., Earl, N., et al. 2022, *ApJ*, 935, 167, doi: [10.3847/1538-4357/ac7c74](https://doi.org/10.3847/1538-4357/ac7c74)
- Protopapa, S., Stansberry, J., Wong, I., et al. 2023, *Bulletin of the AAS*, 55
- Quickenden, T. I., Matich, A. J., Bakker, M. G., Freeman, C. G., & Sangster, D. F. 1991, *The Journal of Chemical Physics*, 95, 8843, doi: [10.1063/1.461217](https://doi.org/10.1063/1.461217)
- Rathbun, J. A., Rodriguez, N. J., & Spencer, J. R. 2010, *Icarus*, 210, 763
- Raut, U., Protopapa, S., Mamo, B. D., et al. 2024, in *EGU General Assembly Conference Abstracts*, EGU General Assembly Conference Abstracts, 6579, doi: [10.5194/egusphere-egu24-6579](https://doi.org/10.5194/egusphere-egu24-6579)
- Rayner, J. T., Toomey, D. W., Onaka, P. M., et al. 2003, *Publications of the Astronomical Society of the Pacific*, 115, 362, doi: [10.1086/367745](https://doi.org/10.1086/367745)
- Robitaille, T. P., Tollerud, E. J., Greenfield, P., et al. 2013, *A&A*, 558, A33, doi: [10.1051/0004-6361/201322068](https://doi.org/10.1051/0004-6361/201322068)
- Spencer, J. R. 1987, PhD thesis, University of Arizona, Tucson, AZ
- Spencer, J. R., Tamppari, L. K., Martin, T. Z., & Travis, L. D. 1999, *Science*, 284, 1514
- Strazzulla, G., Leto, G., Spinella, F., & Gomis, O. 2005, *Astrobiology*, 5, 612, doi: [10.1089/ast.2005.5.612](https://doi.org/10.1089/ast.2005.5.612)
- Teolis, B. D., Plainaki, C., Cassidy, T. A., & Raut, U. 2017, *Journal of Geophysical Research: Planets*, 122, 1996, doi: <https://doi.org/10.1002/2017JE005285>
- Trumbo, S. K., & Brown, M. E. 2023, *Science*, 381, 1308, doi: [10.1126/science.adg4155](https://doi.org/10.1126/science.adg4155)
- Trumbo, S. K., Brown, M. E., & Butler, B. J. 2017a, *The Astronomical Journal*, 154, 148
- . 2018, *The Astronomical Journal*, 156, 161, doi: [10.3847/1538-3881/aada87](https://doi.org/10.3847/1538-3881/aada87)
- Trumbo, S. K., Brown, M. E., Fischer, P. D., & Hand, K. P. 2017b, *The Astronomical Journal*, 153, 250
- Trumbo, S. K., Brown, M. E., & Hand, K. P. 2019a, *Science Advances*, 5, eaaw7123, doi: [10.1126/sciadv.aaw7123](https://doi.org/10.1126/sciadv.aaw7123)
- . 2019b, *The Astronomical Journal*, 158, 127, doi: [10.3847/1538-3881/ab380c](https://doi.org/10.3847/1538-3881/ab380c)
- Trumbo, S. K., Becker, T. M., Brown, M. E., et al. 2022, *The Planetary Science Journal*, 3, 27
- Trumbo, S. K., Brown, M. E., Bockelée-Morvan, D., et al. 2023, *Science Advances*, 9, eadg3724, doi: [10.1126/sciadv.adg3724](https://doi.org/10.1126/sciadv.adg3724)
- USGS. 2002, Controlled photomosaic map of Europa Je 15 M CMN, Report 2757, doi: [10.3133/i2757](https://doi.org/10.3133/i2757)
- Vacca, W. D., Cushing, M. C., & Rayner, J. T. 2003, *Publications of the Astronomical Society of the Pacific*, 115, 389, doi: [10.1086/346193](https://doi.org/10.1086/346193)
- van der Walt, S., Schönberger, J. L., Nunez-Iglesias, J., et al. 2014, *PeerJ*, 2, e453, doi: [10.7717/peerj.453](https://doi.org/10.7717/peerj.453)
- Villanueva, G. L., Hammel, H. B., Milam, S. N., et al. 2023, *Science*, 381, 1305, doi: [10.1126/science.adg4270](https://doi.org/10.1126/science.adg4270)
- Virtanen, P., Gommers, R., Oliphant, T. E., et al. 2020, *Nature Methods*, 17, 261, doi: [10.1038/s41592-019-0686-2](https://doi.org/10.1038/s41592-019-0686-2)
- Zheng, W., Jewitt, D., & Kaiser, R. I. 2006, *The Astrophysical Journal*, 648, 753, doi: [10.1086/505901](https://doi.org/10.1086/505901)